



UNIVERSITY OF LEEDS

This is a repository copy of *Tourmaline $40\text{Ar}/39\text{Ar}$ geochronology and thermochronology: Example from Hadean-zircon-bearing siliciclastic metasedimentary rocks from the Yilgarn Craton.*

White Rose Research Online URL for this paper:

<https://eprints.whiterose.ac.uk/198412/>

Version: Accepted Version

Article:

Thern, ER, Blereau, E orcid.org/0000-0001-8850-397X, Jourdan, F et al. (1 more author) (2020) *Tourmaline $40\text{Ar}/39\text{Ar}$ geochronology and thermochronology: Example from Hadean-zircon-bearing siliciclastic metasedimentary rocks from the Yilgarn Craton.* *Geochimica et Cosmochimica Acta*, 277. pp. 285-299. ISSN 0016-7037

<https://doi.org/10.1016/j.gca.2020.03.008>

© 2020 Elsevier Ltd. This is an author produced version of an article published in *Geochimica et Cosmochimica Acta*. This manuscript version is made available under the CC-BY-NC-ND 4.0 license <http://creativecommons.org/licenses/by-nc-nd/4.0/>. Uploaded in accordance with the publisher's self-archiving policy.

Reuse

This article is distributed under the terms of the Creative Commons Attribution-NonCommercial-NoDerivs (CC BY-NC-ND) licence. This licence only allows you to download this work and share it with others as long as you credit the authors, but you can't change the article in any way or use it commercially. More information and the full terms of the licence here: <https://creativecommons.org/licenses/>

Takedown

If you consider content in White Rose Research Online to be in breach of UK law, please notify us by emailing eprints@whiterose.ac.uk including the URL of the record and the reason for the withdrawal request.



eprints@whiterose.ac.uk
<https://eprints.whiterose.ac.uk/>

Journal Pre-proofs

Tourmaline $^{40}\text{Ar}/^{39}\text{Ar}$ geochronology and thermochronology: Example from the youngest Hadean-zircon-bearing siliciclastic metasedimentary rocks from the Yilgarn Craton

Eric R. Thern, Eleanore Blereau, Fred Jourdan, David R. Nelson

PII: S0016-7037(20)30169-1

DOI: <https://doi.org/10.1016/j.gca.2020.03.008>

Reference: GCA 11685

To appear in: *Geochimica et Cosmochimica Acta*

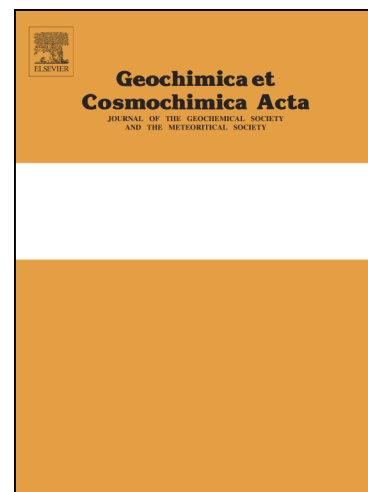
Received Date: 31 July 2019

Accepted Date: 8 March 2020

Please cite this article as: Thern, E.R., Blereau, E., Jourdan, F., Nelson, D.R., Tourmaline $^{40}\text{Ar}/^{39}\text{Ar}$ geochronology and thermochronology: Example from the youngest Hadean-zircon-bearing siliciclastic metasedimentary rocks from the Yilgarn Craton, *Geochimica et Cosmochimica Acta* (2020), doi: <https://doi.org/10.1016/j.gca.2020.03.008>

This is a PDF file of an article that has undergone enhancements after acceptance, such as the addition of a cover page and metadata, and formatting for readability, but it is not yet the definitive version of record. This version will undergo additional copyediting, typesetting and review before it is published in its final form, but we are providing this version to give early visibility of the article. Please note that, during the production process, errors may be discovered which could affect the content, and all legal disclaimers that apply to the journal pertain.

© 2020 Published by Elsevier Ltd.



Tourmaline $^{40}\text{Ar}/^{39}\text{Ar}$ geochronology and thermochronology:

Example from the youngest Hadean-zircon-bearing siliciclastic
metasedimentary rocks from the Yilgarn Craton

Eric R. Thern^{1,2*}, Eleanore Blereau³, Fred Jourdan^{1,3}, and David R. Nelson²

¹Western Australian Argon Isotope Facility, School of Earth and Planetary Sciences, Curtin University, GPO Box U1987, Perth, Western Australia 6845, Australia,

²Geochron Research Group, PO Box 454, Bentley, WA 6982, Australia

³John de Laeter Centre, Curtin University, Perth, WA 6945, Australia

*Corresponding Author: eric@thern.org

ABSTRACT

We present $^{40}\text{Ar}/^{39}\text{Ar}$ ages and boron isotopes of tourmalines from a quartz-tourmaline intrusion cross-cutting the Hadean detrital-zircon-bearing metasedimentary rocks from the Mt. Alfred and Brooking Hills localities of the Illaara Greenstone Belt, Western Australia. Concordant $^{40}\text{Ar}/^{39}\text{Ar}$ plateau ages on the tourmalines at Mt. Alfred give a weighted mean age of 2935 ± 9 Ma (2σ). These results are the first reported Archean $^{40}\text{Ar}/^{39}\text{Ar}$ ages directly obtained on tourmaline, and provide a minimum depositional age for this sequence, placing constraints on the depositional timing of detrital Hadean zircons to between 2935 ± 9 Ma and c.a. 3250 Ma (youngest detrital zircon age in sequence). This is the last known occurrence of abundant detrital Hadean zircons having been directly deposited in a sedimentary sequence, and thus suggests that most Hadean zircon sources have been exhausted by this time. The 2935 ± 9 Ma tourmalines occur within a quartz-tourmaline intrusion with associated stratiform layers and veins, inferred to have grown during a hydrothermal fluid circulation event. A younger generation of tourmalines from the Brooking Hills, 30km south of Mt. Alfred yielded concordant $^{40}\text{Ar}/^{39}\text{Ar}$ plateau ages with a weighted mean age of 2624 ± 16 Ma. These tourmalines occur within and along the margins of post-kinematic quartz veins, parallel to the foliation fabric and marks the end stage of high temperature tectono-thermal events within the Illaara Greenstone Belt. The retention of 2935 ± 9 Ma tourmaline ages within the Illaara Greenstone Belt shows that the K/Ar system of tourmaline remained closed throughout repeated upper-greenschist metamorphic events ($\sim 450^\circ\text{C}$) between the ages of c.a. 2930 to 2630 Ma by opposition to muscovite recording plateau ages of ~ 2.6 Ga. This is in agreement with an approximate Ar closure temperature between $\sim 534\text{--}628^\circ\text{C}$ experimentally determined in this study.

1.0 INTRODUCTION AND GEOLOGICAL SETTING

Tourmaline is a common detrital and hydrothermal mineral, and is abundant in many rock types

throughout the world (Dutrow and Henry, 2011). The robust nature of tourmaline allows for the retention of distinct boron isotopic signatures and integration of fluid inclusions, useful for many studies into the host environment of B-rich fluids and determination of P - T paths of the tourmaline host rocks (van Hinsberg et al., 2011; Marschall and Jiang, 2011). Boron isotopic signatures within tourmaline are also commonly used in many studies to help constrain the hydrothermal fluid sources, and potential depositional environment of source rocks (Harras and El-Sharkawy, 2001). While incredibly useful when used with other minerals to provide age constraints, tourmaline has yet to be a commonly used directly-dated mineral.

Successful dating studies on tourmaline are scarce, with two recent studies using the $^{40}\text{Ar}/^{39}\text{Ar}$ technique on young c.a. 300–400 Ma tourmalines (Bea et al., 2009; Martínez-Martínez et al., 2010). For successful dating via the argon technique, there has to be enough potassium incorporated into the crystal structure to measure radiogenic argon (McDougall and Harrison, 1999). Tourmaline incorporates very small amounts of K, <0.05 weight %, within its structure during crystal formation within the crystallographic X-site. The low energy electron capture decay of ^{40}K to ^{40}Ar produces very little energy, and hence negligible lattice damage to the crystal structure, hindering the formation of fast transport diffusion pathways for quick argon migration or loss. Obtaining meaningful argon results on tourmaline requires avoiding growth zones, inclusions, altered zones, and obtaining tourmaline from rocks that haven't been heated above the closure temperature. The closure temperature of Ar in tourmaline is not well constrained and has yet to be experimentally determined, however it is suspected to be higher than hornblende; c.a. 550°C (McDougall and Harrison, 1999) based on comparison of K/Ar ages of tourmaline, hornblende and muscovite (Andriessen et al., 1991).

The Yilgarn Craton of Western Australia, the source of the tourmalines for this study, is composed of linear, N-S-trending belts of 3000 to 2900 Ma and 2700 to 2650 Ma greenstones separated by late Archaean monzogranite and higher-grade terranes of granitic gneiss such as the

Narryer Terrane in the NW (Figure 1). Greenstone belts within the central and north-western part of the Yilgarn Craton include lenses of metamorphosed sandstone, some of which have yielded detrital zircons with ages in excess of c.a. 4300 Ma at Mt. Narryer and Jack Hills (Trail et al., 2013), Maynard Hills (Nelson, 2002; Wyche et al., 2004), and Mt. Alfred (Nelson, 2005; Thern and Nelson, 2012). These detrital zircons have been extensively studied (Trail et al., 2013), however, their precise depositional timing is currently not well constrained, with a wide range of maximum depositional ages for the sedimentary units they are found within (Rasmussen et al., 2010; Iizuka et al., 2011), and no firm minimum depositional ages.

This study aims to: (i) obtain $^{40}\text{Ar}/^{39}\text{Ar}$ ages on separated Archean tourmalines and investigate their boron isotopic makeup to provide insight into the geological environment they formed within, (ii) determine the diffusion characteristics of Ar within tourmaline crystals and (iii) assess the availability of Hadean zircon sources in the geological record (i.e. Hadean terranes).

2.0 SAMPLE SELECTION AND FIELD RELATIONS

Sample sites at the Brooking Hills, Mt. Alfred within the Illaara Greenstone Belt are composed of metamorphosed sedimentary rocks, including banded iron formations (BIFs) and rhythmites, metasediments, metapelites and greenschists. Outcrops have N–S trending planar-foliation fabrics that are aligned parallel to the Edale and Evanston shear zones. Tourmalines were separated from four samples collected near the sample sites of Mt. Alfred (sample labels 'MA') and the Brooking Hills (sample labels 'BH') shown in Figure 1 (inset Mt. Alfred and Brooking Hills simplified geological sketch maps). Samples MA05, MA08 and MA24 were collected east of Mt. Alfred within the central northern Illaara Greenstone Belt. Samples BH01, BH04 and BH05 were collected at the northern extension of the Brooking Hills, within the centre of the Illaara Greenstone Belt.

2.1 Sample MA05

Muscovite sampling site MA05 (S 28°50.678' E 119°59.965') consists of a fine to medium-grained greenish-white quartzite with minor muscovite/fuchsite laths. The mica laths are aligned to a 4cm thick bedding parallel foliation on the eastern margin of this 20 m-thick outcrop.

2.2 Sample MA08

Tourmaline sampling site MA08 (S 28°50.590' E 120°00.020') consists of a multi-textural assemblage of three contrasting types of tourmaline-bearing rock. The first type is a major, 3x6 meter elongate-along-strike massive hydrothermally-derived intrusion of quartz-tourmaline rock consisting of approximately 25% tourmaline (50–400 μm crystals) and 75% quartz, cross-cut by many quartz veins. The second type is distributed along the margins of this intrusion and throughout the bedding planes along strike of the outcrop consisting of laths of up to 100% tourmalines, as well as recrystallized tourmaline phenocrysts up to 4–10 cm in length and 1–4 cm wide (Figure 2a,b). Some of these form large boudinaged masses elongated along the shearing fabric. The third textural type occurs as 2–5 cm thick quartz-tourmaline blocks (~30% tourmaline, 70% quartz) with 3–5 mm bedding parallel layers that may be related to tectonic shearing. These are boudinaged between layers of siliciclastic metasedimentary rocks as well as some quartz veins.

Tourmalines of the first type are not aligned with the foliation fabrics at sample site MA08 (Figure 2c), whereas the last two types are commonly aligned or elongated within the foliation fabric and folding, and exhibit new growths of acicular elongate 1 cm-long crystals commonly fragmented and deformed around quartz-tourmaline boudinages within the marginal quartz veining.

2.3 Sample MA24

Tourmalines from sample site MA24 (S 28°50.395' E 120°00.042') form a parallel outcrop about 75 meters to the south of the massive quartz-tourmaline vein at site MA08, and are composed primarily

or mm to cm size stratiform tourmaline layers (Figure 2a). These layers appear throughout the Mt.

Alfred locality, and are often 1–2 cm in size and elongated parallel to the foliation fabric. The sample site for samples MA24 principally composed of siliciclastic sedimentary rock that contains alternating fine-grained quartz and quartz-tourmaline layers on a mm to cm scale. These tourmalines are often aligned with the foliation fabric and are between 0.3–0.5 mm in size.

2.4 Samples BH01, BH04 and BH05

Samples BH01/04 (S 28°56.681' E 120°00.040'; Figure 2e) and BH05 (S 28°56.699' E 120°00.021') were collected from near the Brooking Hills (sample labels "BH") in the central part of the Illaara Greenstone Belt from small, 1 to 2 cm wide stratiform quartz-tourmaline veins. Samples are referred to herein as 'metasedimentary rocks', but all have undergone at least greenschist to mid-amphibolite facies metamorphism and nearly all original sedimentary features have been lost due to shearing and late stage metamorphic recrystallization, and is compounded by growth of metamorphic minerals such as muscovite and fuchsite.

An example of this is shown in Figure 3, which shows an overview field photo with shearing fabric and a quartz-tourmaline stratiform vein (centre). The inset close-up photo shows the quartz vein which lies parallel with the siliciclastic metasedimentary rock 'bedding' plane (label 'a') with growth of tourmalines (1.0–3.0 mm) on the margins of this quartz vein (labels 'b' and 'c'). Similar "edge" growth of tourmalines is also displayed along the margins of sample site MA08, where large (mm to cm), acicular crystal growths have formed within fresh quartz veining during later stage SiO₂ fluid circulation. These tourmaline growths are often aligned with the foliation fabric and 'bedding' planes as seen in the siliciclastic metasedimentary rock units. This veining along pre-existing quartz-tourmaline stratiform veins suggests that fluid flow was enhanced along these, likely weaker foliation fabric planes.

3.0 METHODS

3.1 Sample Preparation

Approximately 5kg of sample was crushed via a conventional jaw-crusher and disc mill to reduce fragment size, sieved through a 500 μ m mesh to standardize grain size, and processed over a Wilfley table to remove the bulk of the quartz and produce 250 grams of heavy mineral separates. The resulting material was processed through heavy liquid and magnetic separation to separate out the bulk of the zircons from other heavy minerals present in the samples. These were then sieved into size fractions of >200 μ m, >100 μ m, and <100 μ m, respectively, and tourmalines were picked from the largest fraction.

Tourmalines were separated for $^{40}\text{Ar}/^{39}\text{Ar}$ analysis by manually separating the cleanest sample into a c.a. 20 mg aliquot. After hand picking the cleanest tourmaline crystals (without obvious inclusions, cracks, or core-rim zones) with an optical microscope, the selected tourmalines were leached in diluted HF for one minute and then thoroughly rinsed with distilled water in an ultrasonic cleaner. Tourmalines from the massive vein (sample MA08) and stratiform veins (samples MA24 and BH04) were mounted in epoxy resin discs and polished to about a third of the way through the surface of each grain for boron isotopic analysis on a Cameca IMS 5fE7 ion microprobe. After thorough cleaning, drying, and gold coating, the mount was imaged by reflected and transmitted optical light in order to discern the most obvious cracks, inclusions, cores, and other structures prior to analysis.

3.2 $^{40}\text{Ar}/^{39}\text{Ar}$ Tourmaline and Muscovite Analysis

Samples were loaded into 5 large wells of one 1.9 cm diameter and 0.3 cm depth aluminium disc. These wells were bracketed by small wells that included GA1550 biotite used as a neutron fluence monitor for which an age of 99.77 ± 0.11 Ma was adopted, and a good in-between grain reproducibility has been demonstrated (Renne et al., 1998, 2010). The discs were Cd-shielded (to

minimize undesirable nuclear interference reactions) and irradiated for 25 hours in the Hamilton McMaster University nuclear reactor (Canada) in position 5C. The mean J-values computed from standard grains within the small pits range from 0.0026752 ± 0.0000040 (0.15%) to 0.0026644 ± 0.000054 (0.20%) determined as the average and standard deviation of J-values of the small wells for each irradiation disc. Mass discrimination was monitored using an automated air pipette and provided a mean value of 1.00646 ± 0.00238 per dalton (atomic mass unit). The correction factors for interfering isotopes were $(^{39}\text{Ar}/^{37}\text{Ar})\text{Ca} = 7.30 \times 10^{-4}$ ($\pm 11\%$), $(^{36}\text{Ar}/^{37}\text{Ar})\text{Ca} = 2.82 \times 10^{-4}$ ($\pm 1\%$) and $(^{40}\text{Ar}/^{39}\text{Ar})\text{K} = 6.76 \times 10^{-4}$ ($\pm 32\%$).

$^{40}\text{Ar}/^{39}\text{Ar}$ analyses were performed at the Western Australian Argon Isotope Facility (WAAIF) at Curtin University, operated as part of the John De Laeter Centre for Isotope Research. The laser package samples were step-heated using a 110 W Spectron Laser System, with a continuous Nd-YAG (IR; 1064 nm) laser rastered over the sample for 1 minute to ensure homogeneously distributed temperature. The gas was purified in a stainless-steel extraction line using a GP50 and two AP10 SAES getters and a liquid nitrogen condensation trap. Ar isotopes were measured in static mode using a MAP 215-50 mass spectrometer (resolution of c.a. 450; sensitivity of 4×10^{-14} mol/V) with a Balzers SEV 217 electron multiplier mostly using 9 to 10 cycles of peak-hopping. The data acquisition was performed with the Argus program written by M.O. McWilliams and ran under a LabView environment. The raw data were processed using the ArArCALC software (Koppers, 2002) and the ages have been calculated using the decay constants recommended by (Renne et al., 2010). Blanks were monitored every 3 to 4 steps and typical ^{40}Ar blanks range from 1×10^{-16} to 2×10^{-16} mol. Our criteria for the determination of plateau are as follows: plateaus must include at least 70% of ^{39}Ar . The plateau should be distributed over a minimum of 3 consecutive steps agreeing at 95% confidence level and satisfying a probability of fit (P) of at least 0.05. Plateau ages are given at the 2σ level and are calculated using the mean of all the plateau steps, each weighted by the inverse variance of their individual analytical error. Mini-

plateaus are defined similarly except that they include between 50% and 70% of ^{39}Ar . Integrated ages (2σ) are calculated using the total gas released for each Ar isotope. Inverse isochrons include the maximum number of steps with a probability of fit ≥ 0.05 . The uncertainties on the $^{40}\text{Ar}^*/^{39}\text{Ar}$ ratios of the monitors are included in the calculation of the integrated and plateau age uncertainties, but not the errors on the age of the monitor and on the decay constant (internal errors only, see discussion in (Min et al., 2000)).

3.3 $^{40}\text{Ar}/^{39}\text{Ar}$ Tourmaline Diffusion

No experiment data currently exist to assess the diffusion kinetic of argon in tourmaline, hence the true closure temperature of this mineral is still unknown. The closure temperature of tourmaline is suspected to be higher than hornblende; ca. 550°C (McDougall and Harrison, 1999) based on comparison of K/Ar ages of tourmaline, hornblende and muscovite (Andriessen et al., 1991). Andriessen et al., (1991) illustrates the high blocking temperature of these minerals but is semi-quantitative. Here, we carried out argon temperature-controlled diffusion experiments in order to better assess the diffusion parameter and closure temperature of tourmaline.

Five tourmaline samples, Mt Alfred site MA08 (2935 ± 9 Ma), and multiple Brooking Hills tourmaline sites (BH03, BH05, BH05S and BH04), all similar to site BH04 (2624 ± 16 Ma), were used for argon diffusion experiments. We took 1 aliquot for each sample except for MA08, where we used multiple aliquots. Each sample included 100–200 grains of stubby to equant ~ 100 – 200 μm diameter (often fragmented) crystals that were picked to avoid fragments affected by alteration or that contained inclusions or tourmaline core. Samples were placed in a copper foil package for the furnace run diffusion experiment.

Data reduction procedures are the same as the tourmaline laser section (as above). However, in contrast to other sample from which a laser was used, these samples were step-heated in a double vacuum high frequency Pond Engineering furnace. The gas was purified in a stainless-steel

extraction line using two AP10 and one GP50 SAES getters and a liquid nitrogen condensation trap. Extraction temperatures were measured using a Pond Engineering thermocouple. Each extraction step last 10 minutes including 2 minutes for ramping up the temperature and 8 minutes in a steady state at the desired temperature. Each step was followed by a drop of temperature of 150°C during mass spectrometer analysis. Ar isotopes were measured in static mode using a MAP 215-50 mass spectrometer as described for the laser experiments. For the diffusion calculation, we use ^{39}Ar as diffusant. ^{37}Ar has been also used as a diffusant for Ca-rich mineral; e.g., Plagioclase; (Cassata et al., 2009), however, in the present case for two of three experiments (BH04diff and MA08diff), ^{37}Ar could not be used as it had completely decayed away at the time of the diffusion measurements that were done more than 6 months after the laser dating analyses. Hence, no age could be extracted from the diffusion analyses as ^{37}Ar is required to correct for Ca interferences on mass ^{36}Ar and ^{39}Ar . To illustrate the reproducible degassing behaviour of tourmaline, we plotted the results as degassing curves (Figure A.1). We used the fraction of ^{39}Ar and the duration of each step to calculate the D value using equation 5.29 in McDougall and Harrison (1999). For each sample, $-\ln(D)$ vs. $10000/T$ values were plotted in an Arrhenius plots (Figure 4). The two diffusion parameters, namely activation energy (E_a) and pre-exponential diffusion factor (D_0), were extracted from the array defined by the data in the Arrhenius plot, until the experiment reached a temperature where the crystals break down and start to melt. We used a crystal size radius of 100 μm and a spherical geometry for the calculation, which approximate well the true shape of the broken crystals (Figure 2). Error on the y-axis intercept (D_0) and slope (E_a) are calculated using a robust regression (Isoplot v3.7; (Ludwig, 2003)) since the scatter in individual data along the regression line is much larger than the uncertainty on individual measurement. Closure temperatures for each sample have been calculated using the formulation of Dodson (1973) and for comparison purposes using a cooling rate of 10 $^\circ\text{C}/\text{Ma}$. Uncertainties for each sample were calculated using a Monte Carlo simulation run on Quantum XLTM software (Scibiorski et al., 2015). This approach allows for the complete

propagation of uncertainties on each value (such as variable grain size) and minimises error correlations. The simulation consisted of 10,000 random trials using a triangular distribution. The generated uncertainties were then used for the calculation of the average measured closure temperature.

3.4 Ion Microprobe Boron Isotopic Analysis

Secondary ion mass spectrometry (SIMS) analyses were undertaken using a Cameca IMS 5fE7 ion microprobe located on the Hawkesbury Campus of the University of Western Sydney. Sample surfaces were conductively coated with a 35 nm thick layer of gold using a Leica EM SCD005 sputter coater. Boron isotopic analyses were performed using an O_2^- primary ion source operated at 10 keV and with a secondary-ion extraction potential of 5 keV, providing a net primary ion impact energy of 15 keV at an incidence angle of 24.6 degrees normal to the sample surface. The secondary ion mass spectrometer slits were set to obtain a mass resolving power to 500 (10% of peak height) and an energy window of 50 keV, with no sample energy offset. The magnetic field of the mass spectrometer was sequentially stepped to direct the species $^{10}B^+$ and $^{11}B^+$ into an electron multiplier to determine their count rates. The analytical data were processed using CONCH (Nelson, 2006) to obtain means and uncertainties.

4.0 RESULTS

4.1 Tourmaline $^{40}Ar/^{39}Ar$ Geochronology

Selected $^{40}Ar/^{39}Ar$ age data, presented in Figure 5 (full data SI Table A to K) show two well-defined plateau ages for sample MA08 laser packages 1 and 2 (Figure 5a, b), and a plateau for the diffusion run within the furnace (Figure 5c; SI Table A and B). The two tourmaline multi-grain laser package $^{40}Ar/^{39}Ar$ plateaus, with ages of 2936 ± 21 Ma (probability $P=0.08$) and 2941 ± 19 Ma ($P=0.09$), show a consistency between duplicate sample runs where $>75\%$ radiogenic ^{39}Ar is represented in

the plateau. K/Ca vs. total ^{39}Ar and Cl/K vs. total ^{39}Ar plots are consistent between our two aforementioned age plateaus (Figure 5a, b). Cl/K only has values over ~ 0 for the first few steps of both analyses. These steps likely relate to argon released from surficial cracks and were not included within the age plateaus. The essentially nil values of Cl/K also indicates a lack of Cl rich fluids that can be potentially associated with excess argon (Baxter et al., 2002). K/Ca shows very consistent values for the age steps incorporated into the plateau age, indicating a lack of Ca-rich inclusions within our tourmaline. Six single-grain tourmaline step-heating experiments (Figure 5, and more in SI Table C-H) yield indistinguishable albeit less precise ages, suggesting that no inherited grains are present. Overall uncertainties for these are higher due to their low K contents (commonly 0.05 weight %) making it hard to date single crystals. The K/Ca ratios (SI Table A-J) show that the tourmaline crystals have relatively homogeneous compositions.

A single-grain analysis of one of the MA24 'stratiform' tourmalines resulted in a plateau age of 3047 ± 128 Ma ($P=0.16$; SI Table H), within analytical uncertainty of the age of 2935 ± 9 Ma obtained on tourmalines from sample MA08.

Individual large (c.a. 0.5–1 mm) tourmalines from Brooking Hills (BH05) yielded younger ages than those of sample MA08. Three individual grains were analysed by $^{40}\text{Ar}/^{39}\text{Ar}$ step-heating, producing two plateau ages of 2617 ± 26 and 2628 ± 20 Ma (shown in SI Table I and J). The average weighted mean age of these two analyses is 2624 ± 16 Ma ($P=0.50$). These tourmalines are generally larger than those from sample MA08, and have grown on the margins of late-stage quartz veins, often parallel to shearing fabric.

4.2 Argon Diffusion in Tourmaline

In addition to the age data presented in this paper, we present diffusion data for six furnace experiments. The Arrhenius plots (Figure 4) show that the ^{39}Ar data usually yield two arrays of data with two distinct slopes before the breakdown of the tourmaline crystals. The shallow array only

includes a few % of the total gas, has a shallow slope and shows very fast diffusivity at low temperature ($\ll 50^\circ\text{C}$). We interpret these data as indicating very fast release of argon by cracks and defects and coming from any potassium located in low retentive cation sites, and will not be considered further in this study. The second array of data points includes most of the gas of each experiment, results in a much steeper slope, and forms the age plateau. This is interpreted to be the release of Ar from the X-site within the tourmaline structure. Furnace data yielded E_a (activation energy) values ranging from $\sim 505\text{--}815$ KJ/mol and D_0 (pre-exponential diffusion factor) average values ranging from $\sim 1.65 \times 10^{15}$ to $\sim 6.95 \times 10^{27}$ cm^2/s for crystals with an average radius of 100 ± 25 μm . From those values, we can calculate individual closure temperatures ranging from 492 ± 93 to 637 ± 61 Ma. To support our diffusion data we compared degassing profiles for other minerals with closure temperatures close to the range we propose for tourmaline (hornblende and biotite) (Figure 6a). We then modelled the expected degassing curves using average E_a and D_0 values in the literature and using the ArArDiff algorithm (Jourdan and Eroglu, 2017). These synthetic curves (Figure 6b) are very similar to the ones we observed in the laboratory, with tourmaline showing the narrowest degassing peak at $\sim 850^\circ\text{C}$, similar to biotite, but noticeably lower than hornblende around $1100\text{--}1200^\circ\text{C}$. These temperatures should not be mistaken for closure temperatures.

4.3 Muscovite $^{40}\text{Ar}/^{39}\text{Ar}$ Geochronology

$^{40}\text{Ar}/^{39}\text{Ar}$ dating of muscovite from Mt Alfred (MA05) and Brooking Hills (BH01) both yielded well defined plateaus ages of 2601 ± 11 Ma ($P = 0.38$) and 2606 ± 11 Ma ($P = 0.88$) respectively, based on $>90\%$ of ^{39}Ar in the plateaus (Figure 7). The consistent nature of the plateaus means that it is very unlikely that they are the product of excess argon that can plague muscovite.

4.4 SHRIMP U-Pb Zircon Geochronology

Zircons from sample MA08, found in lower abundance than the surrounding siliciclastic

metasedimentary rocks, are rounded and pitted, consistent with a detrital origin and their being inherited from the intruded metasedimentary rocks. A summary of ages obtained on 19 zircons are shown in the Wetherill diagram and Gaussian summation probability plots in (Figure 8; data table SI Table N). Zircon analyses, while few, form a main concordant age group consisting of 6 analyses at 3623 ± 10 Ma, as well as a semi-discordant group of 2 analyses at 3726 ± 2 Ma and the youngest nearly-concordant analysis of 3272 ± 2 Ma (Figure 8).

4.5 Boron Isotopes

Boron isotopic results for samples MA24, MA08 and BH04 are shown in Figure 9 (more info in SI Table O) outlining different fields for the formation of tourmaline. The bulk of the analyses on all three samples have a $\delta^{11}\text{B}$ variation between -4.0% $\delta^{11}\text{B}$ to 1.0% $\delta^{11}\text{B}$. Sample MA24 has a broad peak and many analyses below -2.0% $\delta^{11}\text{B}$, sample MA08 shows a bi-modal distribution above and below -4.0% $\delta^{11}\text{B}$ which mostly relates to cores (enriched $\delta^{11}\text{B}$) and rims (depleted $\delta^{11}\text{B}$), and sample BH04 shows a simple population ranging from -4.0% $\delta^{11}\text{B}$ to 2.0% $\delta^{11}\text{B}$.

Tourmaline core analyses, as evidenced from SEM microstructural imaging and SIMS, show that some cores have lower $\delta^{11}\text{B}$ values compared to the bulk of the tourmalines. These cores may be linked with $^{40}\text{Ar}/^{39}\text{Ar}$ late stage heating steps that show $\sim 5\text{--}10\%$ ^{39}Ar around c.a. 3050–3100 Ma. It has yet to be determined whether these cores are in fact detrital and picked up during intrusion, or whether they are formed from an earlier fluid fluxing event. Most of the tourmalines fall within the carbonates and evaporites field, and the decompression and prograde field of tourmaline formation. All analyses are enriched in heavy boron ^{11}B relative to the continental crust.

5.0 DISCUSSION

5.1 Tourmaline Age and Characteristics

Age summary

Our results show that tourmaline is a good candidate mineral for $^{40}\text{Ar}/^{39}\text{Ar}$ geochronology when proper care is taken to pick only inclusion-free grains. We obtained 9 concordant plateau ages for tourmaline from Mt Alfred, resulting in a weighted mean age of 2935 ± 9 Ma ($P = 0.57$). The younger generation of tourmaline at Brooking Hills yielded two plateau ages with a weighted mean of 2624 ± 16 Ma ($P=0.50$).

Diffusion parameters

The diffusion experiments produced a range of E_a (~ 505 – 815 KJ/mol) and D_0 ($\sim 1.65 \times 10^{15}$ to $\sim 6.95 \times 10^{27}$ cm^2/s) values that are highly correlated, producing a range of values that result in linear regression line. Using a combination of correlated, uncorrelated and average values we calculated similar, yet discordant, weighted mean closure temperature values. The best first estimate of the closure temperature is through a weighted mean of the measured experimental temperatures coupled with the associated uncertainties generated through Monte Carlo simulations. This calculation produces a closure temperature range of 534 – 628°C with a mean of $\sim 580^\circ\text{C}$ (95%; $\text{MSWD} = 4.9$; $P = 0.0$; $n = 7$); calculated using the largest uncertainty for each individual measurement, and for a cooling rate of $10^\circ\text{C}/\text{Ma}$. However, the mean closure temperature should only be used as a semi-quantitative value as the data presented here are discordant as indicated by a very low P -value and high MSWD , so those are just the first steps in precisely measuring the diffusion parameters of tourmaline for various compositions and types of tourmalines. The reason for the discordance between results is not clear. Is there a natural variation of closure temperature due to the structure of tourmaline, or perhaps affected by fast diffusion pathways? There is also the problem of dehydroxylation during in vacuo experiments which can lead to erroneous data and will be addressed in the next section.

The problem of structural change and dehydroxylation in hydrous minerals.

When undergoing incremental heating analysis in vacuo, hydrous minerals are particularly vulnerable to phase transformations which can affect the release of gas from the mineral and thus its diffusion kinetics (Lee et al., 1991; Harrison et al., 2009; Cassata and Renne, 2011; Ren and Vasconcelos, 2019). Structural changes means that one may not be measuring the kinetics of volume diffusion of a particular crystal but of a modified version of such a crystal. Dehydroxylation (the loss of the hydroxyl group OH during heating) causes an important phase change in hydrous minerals such as tourmaline and occurs under vacuum at relatively low extraction temperatures of a few hundreds of degrees Celsius and between 600 and 900°C at atmospheric pressure (Gonzalez-Carreno et al., 1988). For comparison, the bulk of the gas extraction of the tourmaline samples analysed in this study occurs between 800 and 900°C, most certainly above the dehydroxylation temperature of tourmaline. In natural geological settings at elevated lithostatic pressure, however, those minerals will stay well below the dehydroxylation temperature during most metamorphic episodes, thus the diffusion parameters measured in the laboratory will most likely not be applicable to the original mineral and thus limit their applicability to thermal history reconstructions (Harrison et al., 2009; Ren and Vasconcelos, 2019). A better approach to measure the diffusion parameters of a hydrated mineral is to conduct hydrothermal diffusion experiments to allow the crystal structure to stay stable at higher temperature (e.g.; Harrison et al., 2009). Such an approach was unfortunately not feasible during the course of this study. Thus, dehydroxylation might be in fact the cause of the scatter in the diffusion parameters and closure temperature measured in this study (Gaber et al., 1988).

Another structural change that have been observed during heating of tourmaline is a tightening of the crystal structure or from de-boronization which both occurs above 950°C (Wang et al., 2018; Deer et al., 1997, pg 584). However, since most of the argon is released in between 800 and 900°C (Fig. 6a), this process alone does not affect our ability to measure the Ar kinetics in tourmaline.

In conclusion, the range of E_a and D_0 values measured in this study should be taken as informative

and semi-quantitative and not to be used for precise time-temperature history reconstruction and future work in the form of hydrothermal experiments should be carried out to refine the diffusional properties of argon in tourmaline. Nevertheless, we believe that these values are not far off from the true diffusion values of tourmaline for reasons that will be given in the following discussion.

Support for the approximate E_a and D_0 values calculated in this study

Muscovite-bearing quartzite sampled in close proximity (<100 m) to the 2.9 Ga tourmaline-bearing samples underwent the same temperature conditions as tourmaline, yet yielded two well-defined plateau ages of 2601 ± 11 and 2606 ± 11 Ma much younger than tourmaline. This region underwent several upper-greenschist to mid-amphibolite facies ($\sim 450^\circ\text{C}$) events between 2.6 and 2.9 Ga, with a thermal peak at c.a. 2730 Ma (Nelson, 2001; Chen et al., 2003, 2004), with muscovite giving consistently younger ages across the region (Jourdan et al., 2014). This evidence, coupled with no evidence for Cl-rich fluid potentially carrying excess argon ($\text{Cl/K} = \sim 0$; Fig. 5a, b) and the flat nature of the age spectra lacking any significant indication of ^{40}Ar loss at 2.6 Ga (Fig. 5), lends support to the closure temperature of tourmaline being significantly above $\sim 450^\circ\text{C}$, the closure temperature of muscovite (Harrison et al., 2009) and estimated peak metamorphic conditions (Nelson, 2001) hence compatible with a value $>530^\circ\text{C}$.

Fig. 6a shows degassing curves measured in the laboratory for tourmaline, biotite and hornblende whereas Fig 6b shows similar curves as modelled using the algorithm ArArDIFF coupled with E_a and D_0 values either measured in this study (tourmaline) or from literature based on hydrothermal experiments (hornblende and biotite; recalculated by Scibiorski et al., 2015). Fig. 6 shows that the measured and synthetic curves are approximately in the right location compared to each other lending additional support for our diffusion values. Tourmaline modelled curve predicts that tourmaline should release most of its gas between c.a. 700 and 900°C , in comparison with laboratory heating experiments showing an actual narrower temperature range between 800 and

900°C. This slight discrepancy may in fact indicate that the closure temperature of tourmaline might be located toward the higher temperature portion of the 534–628 °C range calculated in this study.

More work is also required to determine if this value is composition dependent as observed for feldspar (Cassata and Renne, 2013). Nevertheless, our experiments give a good indication on the Ar retention propriety of tourmaline with a closure temperature somewhat around 500–600°C, making tourmaline a highly Ar-retentive mineral that can be used for $^{40}\text{Ar}/^{39}\text{Ar}$ dating and thermochronology. Lastly, those values should not be surprising as tourmaline is known for its extremely low diffusion rate for other elements (Marschall and Jiang, 2011).

Implications for thermochronology of tourmaline

The preliminary diffusion data presented in this study suggest that tourmaline is a very retentive mineral, probably similar to amphibole (550°C; McDougall and Harrison, 1999) and orthopyroxene (OPX: ~620°C; Cassata et al., 2011) and osumilite (~620°C; Blereau et al., 2019). Such a high closure/retention temperature, in particular if confirmed to be the standard for all types of tourmaline, makes this crystal ideally suited for studying the high-temperature thermochronology of tourmaline-bearing rocks that are present in a large range of settings (Dutrow and Henry, 2011). In particular, since tourmaline is more likely to grow during the prograde P – T history because of the exhaustion of boron liberation before peak metamorphism (van Hinsberg et al., 2011), $^{40}\text{Ar}/^{39}\text{Ar}$ dating may provide information on the prograde history of a rock provided that the system stays below ~580°C. Peak upper-greenschist to mid-amphibolite grade (~450–550°C) thermal events throughout the Illaara Greenstone Belt at c.a. 2730 Ma (Nelson, 2001; Chen et al., 2003, 2004) have thus not reset the 2935 ± 9 Ma tourmaline ages, in agreement with the upper range of the closure temperature calculated in this study.

5.2 Tourmaline Ages Significance

The older 2955 ± 9 Ma tourmaline age appears to be unusual in that there are no dated rocks of this age within the Illaara Greenstone Belt or in the immediate surrounding area (within ~ 50 km) (Figure 10). In contrast, the Yilgarn Craton as a whole has a number of granitic and volcanic rock occurrences that are close to, or part of, the Yilgarn basement, with ages between c.a. 2960–2920 Ma measured using U–Pb zircon geochronology (labelled on Figure 1, inset Yilgarn Craton). In particular, the western part of the Murchison Domain has a 2960–2920 Ma Golden Grove Group, that is composed of granites and komatiitic and tholeiitic basalts (Wang et al., 1998; Mole et al., 2013; Ivanic et al., 2012). To the south of the Illaara Greenstone Belt is the Penneshaw Formation, a c.a. 2930–2938 Ma formation (Campbell and Hill, 1988) consisting of amphibolites, massive to pillowed basalts, and a minor component of sedimentary and felsic volcanic rocks (Nelson, 1997), and may represent a fragment of the Yilgarn basement, underlying the 2720 Ma Kambalda Sequence (Kositcin et al., 2008). Some porphyritic micro-granite sills have also been dated within the Southern Cross Greenstone Belt at 2934 ± 7 Ma (Mueller and McNaughton, 2000), and the Lake Johnston Greenstone Belt at 2921 ± 4 Ma (Joly et al., 2010). The existence of rocks within the basement of the Yilgarn Craton of similar ages to these tourmalines show that the rocks within the Illaara Greenstone Belt, and throughout the Yilgarn were thermally active during this period - facilitating hydrothermal activity.

These events are part of, or strongly associated with, a lower greenstone basement that was the pre-rifted nucleus components of the now disassociated N–S trending greenstone belts throughout the Yilgarn Craton, including the Illaara Greenstone Belt and the 'basement' siliciclastic metasedimentary rocks that host the tourmaline intrusion at sample site MA08, the similarly aged stratiform offshoots of this at sample site MA24, and the younger quartz veining-related tourmaline sample sites BH04 and BH05. The Hadean zircon-bearing sedimentary rocks were likely associated with these previously mentioned 2960–2920 Ma greenstone sequences, although it currently cannot be determined whether they provided the basement to these sequences.

5.3 Depositional Age Constraints and Implications for Hadean Zircon Source Availability

Stratiform tourmalines occur as post-depositional stratiform layers within the metasedimentary rocks, and have likely grown during a period of enhanced heating and hydrothermal fluid flow. The simpler tectonic and metamorphic history of the Illaara Greenstone Belt compared to that of the Jack Hills has allowed for the determination of a well constrained depositional history. The $^{40}\text{Ar}/^{39}\text{Ar}$ tourmaline age of 2935 ± 9 Ma, the first Archean tourmaline ever directly dated, provides a minimum depositional age for the siliciclastic metasedimentary rocks of the Illaara Greenstone Belt (Figure 10). This age thus constrains the deposition of the original sediments at Mt. Alfred, which also places constraints on the window of Hadean-zircon-bearing sedimentation and availability of Hadean grains to between c.a. 2935 Ma and 3250 Ma (Thern and Nelson, 2012). These metasediments represent the last known occurrence of abundant detrital Hadean zircons having been directly deposited in a sedimentary sequence. This suggests that most Hadean zircon sources or Hadean terranes have been destroyed or recycled by this time.

Boron analyses within all tourmaline samples are enriched in heavy boron ^{11}B relative to the continental crust. The heavy $\delta^{11}\text{B}$ signatures between -4.0% and 2.0% imply that their fluid source was likely from volcano-sedimentary rocks in equilibrium with seawater (Garda et al., 2009), and not derived from the metasedimentary rocks or the continental crust. A non-continental, non-metasedimentary source of fluids is consistent with volcanic activity in the form of basalts (including pillow-flows) throughout the Yilgarn Craton between 2960–2920 Ma (Wang et al., 1998; Campbell and Hill, 1988; Nelson, 1997) and the 2935 ± 9 Ma tourmaline age may be related to formation from heated fluids during a rifting event.

5.4 Late Stage Tourmalines

The tourmalines from the Brooking Hills sample site BH05, with an age of 2624 ± 16 Ma, are

significantly younger than those of sample MA08. Their formation along the margins of quartz veining, as displayed in (Figure 3), suggests either that (i) late-stage quartz vein fluids were B-rich, or (ii) they became B-enriched by interacting with the surrounding metasedimentary rocks via breakdown of local B-rich minerals. Their similar $\delta^{11}\text{B}$ isotopic signatures suggests a common source, or recycling of similar boron rich fluids.

The $^{40}\text{Ar}/^{39}\text{Ar}$ dates obtained for the younger generation of tourmalines correspond to the timing of quartz veining throughout the Illaara Greenstone Belt during semi-ductile to brittle late-stage deformation (See Figure 3; (Chen et al., 2004)). Since quartz veins (some with tourmaline crystallization and some without) cross-cut existing folding and shearing, this age defines the end-stage of high-temperature (300–400°C) metamorphism within the Illaara Greenstone Belt. These younger tourmalines show that this mineral is well suited for the assessment of low-temperature hydrothermal histories during remobilization of B-rich fluids, as revealed by the younger generation of 2624 ± 16 Ma tourmalines identified in this study.

The siliciclastic metasedimentary rocks of the Illaara Greenstone Belt hosting these tourmalines represent rafts of greenstones that have been separated from a potentially common proto-terrane nucleus after c.a. 3000 Ma. These were then incorporated into the Yilgarn Craton by bringing together foreign and neighboring greenstones and associated quartzites between 2935 ± 9 Ma (minimum depositional age for common sandstone/quartzites) and 2624 ± 16 Ma. Late stage shearing at c.a. 2624 ± 16 Ma (Chen et al., 2003) is synchronous with the younger generation of tourmaline formation within the margins of quartz veining and defines the end of greenschist metamorphism and shear zones within the Illaara Greenstone Belt. These two generations of tourmaline thus constrain the start and end of the major tectono-thermal events within the Illaara Greenstone Belt.

6.0 CONCLUSIONS

1) $^{40}\text{Ar}/^{39}\text{Ar}$ tourmaline ages of 2935 ± 9 Ma, the first Archean tourmaline ever directly dated, reveals the minimum depositional age for the siliciclastic metasedimentary rocks of the Illaara Greenstone Belt. This age constrains the deposition of the original sediments at Mt. Alfred, and places limits on Hadean-zircon-bearing source rock availability to weathering and deposition to between 2935 ± 9 Ma and 3250 Ma. This is the last known occurrence of abundant Hadean zircons having been directly deposited in a sedimentary sequence, and thus suggests that most Hadean zircon sources have been exhausted by this time, and by extension could indicate no more Hadean terranes after 2935 Ma.

2) The Mt. Alfred Hadean-zircon bearing siliciclastic metasedimentary rocks have a less complex post-depositional tectonic and metamorphic history than those of the Jack Hills, with a minimum depositional age of 2935 ± 9 Ma, and no major tectono-thermal events younger than 2624 ± 16 Ma.

3) A younger generation of tourmalines from the Brooking Hills, show that late stage hydrothermal quartz-vein fluids remobilized boron and crystallized new tourmalines at 2624 ± 16 Ma. This age, coupled with field relations of quartz-tourmaline veins that cross-cut tectonic shearing fabrics, defines the age of the final major metamorphic and hydrothermal activity within the Illaara Greenstone Belt.

4) Diffusion experiments on argon in tourmaline yield an average semi-quantitative closure temperature of $580 \pm 47^\circ\text{C}$. These results suggest that tourmaline is among the most Ar-retentive minerals, and will retain a crystallization age even after upper-greenschist to mid-amphibolite facies metamorphic events.

5) Dating tourmaline by the $^{40}\text{Ar}/^{39}\text{Ar}$ technique offers a unique approach to the resolution of complex geological relationships and P – T histories within many geological contexts, including Archean metasedimentary environments, previously closed to geochronological investigation.

ACKNOWLEDGMENTS

We thank Adam Frew for help during field work and technical support. Adam Frew and Celia Mayers for their help during Ar-lab sample preparation and coordination.

REFERENCES CITED

- Andriessen, P.A.M., Hebeda, E.H., Simon, O.J., and Verschure, R.H. (1991) Tourmaline KAr ages compared to other radiometric dating systems in Alpine anatectic leucosomes and metamorphic rocks (Cyclades and southern Spain). *Chemical Geology* 91, 33–48.
- Baxter, E.F., DePaolo, D.J., and Renne, P.R. (2002) Spatially correlated anomalous $^{40}\text{Ar}/^{39}\text{Ar}$ “age” variations in biotites about a lithologic contact near Simplon Pass, Switzerland: A mechanistic explanation for excess Ar. *Geochimica et Cosmochimica Acta* 66, 1067–1083.
- Bea, F., Pesquera, A., Montero, P., Torres-Ruiz, J., and Gil-Crespo, P.P. (2009) Tourmaline $^{40}\text{Ar}/^{39}\text{Ar}$ chronology of tourmaline-rich rocks from Central Iberia dates the main Variscan deformation phases. *Geologica Acta* 7, 399–412.
- Blereau, E., Clark, C., Jourdan, F., Johnson, T.E., Taylor, R.J.M., Kinny, P.D., Danišík, M., Hand, M., and Eroglu, E. (2019) Closed system behavior of argon in osumilite records protracted high-temperature metamorphism within the Rogaland-Vest Agder Sector, Norway. *Journal of Metamorphic Geology* 37, 667–680.
- Campbell, I.H., and Hill, R.I. (1988) A two-stage model for the formation of the granite-greenstone terrains of the Kalgoorlie-Norseman area, Western Australia. *Earth and Planetary Science*

- Cassata, W.S., and Renne, P.R. (2013) Systematic variations of argon diffusion in feldspars and implications for thermochronometry. *Geochimica et Cosmochimica Acta* 112, 251–287.
- Cassata, W.S., Renne, P.R., and Shuster, D.L. (2011) Argon diffusion in pyroxenes: Implications for thermochronometry and mantle degassing. *Earth and Planetary Science Letters* 304, 407–416.
- Cassata, W.S., Renne, P.R., and Shuster, D.L. (2009) Argon diffusion in plagioclase and implications for thermochronometry: A case study from the Bushveld Complex, South Africa. *Geochimica et Cosmochimica Acta* 73, 6600–6612.
- Chen, S.F., Libby, J.W., Wyche, S., and Riganti, A. (2004) Kinematic nature and origin of regional-scale ductile shear zones in the central Yilgarn Craton, Western Australia. *Tectonophysics* 394, 139–153.
- Chen, S.F., Riganti, A., Wyche, S., Greenfield, J.E., and Nelson, D.R. (2003) Lithostratigraphy and tectonic evolution of contrasting greenstone successions in the central Yilgarn Craton, Western Australia. *Archaean Tectonics* 127, 249–266.
- Chen, S.F., Witt, W.K., and Liu, S. (2001) Transpression and restraining jogs in the northeastern Yilgarn craton, Western Australia. *Precambrian Research* 106, 309–328.
- Deer, W.A., Howie, R.A. and Zussman, J. (1997) *Rock-Forming Minerals: Disilicates and Ring Silicates*. Geological Society of London.
- Dodson, M.H. (1973) Closure temperature in cooling geochronological and petrological systems. *Contributions to Mineralogy and Petrology* 40, 259-274.
- Dutrow, B.L., and Henry, D.J. (2011) *Tourmaline: A Geologic DVD*. *Elements* 7, 301–306.

- Gaber, L.J., Foland, K.A. and Corbato, C.E. (1988) On the significance of argon release from biotite and amphibole during $40\text{Ar}/39\text{Ar}$ vacuum heating. *Geochimica et Cosmochimica Acta* 52, 2457-2465.
- Garda, G.M., Trumbull, R.B., Beljavskis, P., and Wiedenbeck, M. (2009) Boron isotope composition of tourmalinite and vein tourmalines associated with gold mineralization, Serra do Itaberaba Group, central Ribeira Belt, SE Brazil. *Chemical Geology* 264, 207–220.
- Gonzalez-Carreño, T., Fernández, M., Sanz, J. (1988) Infrared and electron microprobe analysis of tourmalines. *Physics and Chemistry of Minerals* 15, 452-460.
- Harraz, H.Z., and El-Sharkawy, M.F. (2001) Origin of tourmaline in the metamorphosed Sikait pelitic belt, south Eastern Desert, Egypt. *Journal of African Earth Sciences* 33, 391–416.
- Harrison, T. M., Célérier, J., Aikman, A.B., Hermann, J., Heizler, M. (2009) Diffusion of ^{40}Ar in muscovite. *Geochimica et Cosmochimica Acta* 73, 1039-1051.
- Van Hinsberg, V.J., Henry, D.J., and Dutrow, B.L. (2011) Tourmaline as a Petrologic Forensic Mineral: A Unique Recorder of Its Geologic Past. *Elements* 7, 327–332.
- Iizuka, T., Nebel, O., and McCulloch, M.T. (2011) Tracing the provenance and recrystallization processes of the Earth's oldest detritus at Mt. Narryer and Jack Hills, Western Australia: An in situ Sm-Nd isotopic study of monazite. *Earth and Planetary Science Letters* 308, 350–358.
- Ivanic, T.J., Van Kranendonk, M.J., Kirkland, C.L., Wyche, S., Wingate, M.T.D., and Belousova, E.A. (2012) Zircon Lu–Hf isotopes and granite geochemistry of the Murchison Domain of the Yilgarn Craton. *Lithos* 148, 112–127.
- Joly, A., Miller, J., and McCuaig, T.C. (2010) Archean polyphase deformation in the Lake Johnston

Craton. *Precambrian Research* 177, 181–198.

Jourdan, F. and Eroglu, E. (2017) $^{40}\text{Ar}/^{39}\text{Ar}$ and (U-Th)/He model age signatures of elusive Mercurian and Venusian meteorites. *Meteoritics and Planetary Science* 52, 884-905.

Jourdan, F., Frew, A., Joly, A., Mayers, C., and Evans, N. (2014) WA1ms: A ~2.61 Ga muscovite standard for $^{40}\text{Ar}/^{39}\text{Ar}$ dating. *Geochimica et Cosmochimica Acta* 141, 113-126.

Kositcin, N., Brown, S.J.A., Barley, M.E., Krapez, B., Cassidy, K.F., and Champion, D.C. (2008) SHRIMP U-Pb zircon age constraints on the Late Archaean tectonostratigraphic architecture of the Eastern Goldfields Superterrane, Yilgarn Craton, Western Australia. *Precambrian Research* 161, 5–33.

Koppers, A.A.P. (2002) ArArCALC-software for $^{40}\text{Ar}/^{39}\text{Ar}$ age calculations. *Computers & Geosciences* 28, 605–619.

Lee, J.K.W., Onstott, T.C., Cashman, K.V., Cumbest, R.J., and Johnson, D. (1991) Incremental heating of hornblende in vacuo: Implications for $^{40}\text{Ar}/^{39}\text{Ar}$ geochronology and the interpretation of thermal histories. *Geology* 19, 872-876.

Ludwig, K.R. (2003) Isoplot 3.00: a geochronological toolkit for Microsoft Excel. Berkeley Geochronological Centre Special Publications 4.

Marschall, H.R., and Jiang, S.-Y. (2011) Tourmaline Isotopes: No Element Left Behind. *Elements* 7, 313–319.

Martínez-Martínez, J.M., Torres-Ruiz, J., Pesquera, A., and Gil-Crespo, P.P. (2010) Geological relationships and U-Pb zircon and $^{40}\text{Ar}/^{39}\text{Ar}$ tourmaline geochronology of gneisses and tourmalinites from the Nevado-Filabride complex. *Lithos* 119, 238–250.

McDougal, I., and Harrison, T.M. (1999) Geochronology and Thermochronology by the

$^{40}\text{Ar}/^{39}\text{Ar}$ Method. Oxford University Press, USA.

Min, K., Mundil, R., Renne, P.R., and Ludwig, K.R. (2000) A test for systematic errors in $^{40}\text{Ar}/^{39}\text{Ar}$ geochronology through comparison with U/Pb analysis of a 1.1-Ga rhyolite. *Geochimica et Cosmochimica Acta* 64, 73–98.

Mole, D.R., Fiorentini, M.L., Cassidy, K.F., Kirkland, C.L., Thebaud, N., McCuaig, T.C., Doublier, M.P., Duuring, P., Romano, S.S., Maas, R., Belousova, E.A., Barnes, S.J., and Miller, J. (2013) Crustal evolution, intra-cratonic architecture and the metallogeny of an Archaean craton. Geological Society, London, Special Publications 393.

Mueller, A.G., and McNaughton, N.J. (2000) U-Pb Ages Constraining Batholith Emplacement, Contact Metamorphism, and the Formation of Gold and W-Mo Skarns in the Southern Cross Area, Yilgarn Craton, Western Australia. *Economic Geology* 95, 1231–1257.

Nelson, D.R. (2001) Compilation of geochronology data, 2000. GSWA.

Nelson, D.R. (2002) Compilation of geochronology data, 2001. GSWA.

Nelson, D.R. (2005) Compilation of geochronology data, 2003. GSWA.

Nelson, D.R. (1997) Evolution of the Archaean granite-greenstone terranes of the Eastern Goldfields, Western Australia: SHRIMP U—Pb zircon constraints. *Archaean Granite-Greenstone Geology of the Eastern Goldfields* 83, 57–81.

Nelson, D.R., Robinson, B.W., and Myers, J.S. (2000) Complex geological histories extending for >4.0 Ga deciphered from xenocryst zircon microstructures. *Earth and Planetary Science Letters* 181, 89–102.

geochronology of monazite and xenotime from the Jack Hills belt: Implications for the age of deposition and metamorphism of Hadean zircons. *Precambrian Research* 180, 26–46.

Ren, Z. and Vasconcelos, P.M. (2019) Argon diffusion in hypogene and supergene alunites: Implications to geochronology and thermochronometry on Earth and Mars. *Geochimica et Cosmochimica Acta* 262, 166-187.

Renne, P.R., Mundil, R., Balco, G., Min, K., and Ludwig, K.R. (2010) Joint determination of 40K decay constants and 40Ar*/40K for the Fish Canyon sanadine standard, and improved accuracy for 40Ar/39Ar geochronology. *Geochimica et Cosmochimica Acta* 74, 5349–5367.

Renne, P.R., Swisher, C.C., Deino, A.L., Karner, D.B., Owens, T., and Depaolo, D.J. (1998) Intercalibration of Standards, absolute ages and uncertainties in 40Ar/39Ar dating. *Chemical Geology* 145, 117–152.

E. Scibiorski, E. Tohver, F. Jourdan. (2015) Rapid Mesoproterozoic cooling and exhumation in the western Albany-Fraser Orogen, Western Australia. *Precambrian Research* 265, 232-248.

Thorn, E.R., and Nelson, D.R. (2012) Detrital zircon age structure within ca. 3 Ga metasedimentary rocks, Yilgarn Craton: elucidation of Hadean source terranes by principal component analysis. *Precambrian Research* 214-215, 28–43.

Trail, D., Watson, E.B., and Tailby, N. (2013) Insights into the Hadean Earth from experimental studies of zircon. *Journal of the Geological Society of India* 81, 605–636.

Wang, Q., Schiøtte, L., and Campbell, I.H. (1998) Geochronology of supracrustal rocks from the Golden Grove area, Murchison Province, Yilgarn Craton, Western Australia. *Australian Journal of Earth Sciences* 45, 571–577.

transformation and microstructural evolution of black tourmaline mineral powders during heating and cooling processes. *Ceramics International* 44, 13253-13258.

Wyche, S., Nelson, D.R., and Riganti, A. (2004) 4350–3130 Ma detrital zircons in the Southern Cross Granite–Greenstone Terrane, Western Australia: implications for the early evolution of the Yilgarn Craton. *Australian Journal of Earth Sciences* 51, 31–45.

FIGURE CAPTIONS

Figure 1: Map of the Yilgarn Craton, Western Australia, showing the Maynard Hills and Illaara Greenstone Belts of the Southern Cross Domain with inset maps of the Mt. Alfred (samples MA08, MA24) and Brooking Hills (samples BH04, BH05) sampling localities.

Figure 2: Tourmalines from sample MA08 in an ion-probe mount (A) and as separate grains (B). (A) Selected grains (lower case a) show terminations and crystal facets. Many grains show fluid inclusions. Some grains show core and rim overgrowths (c, r). (B) tourmalines as separate grains, showing surfaces of each grain. Selected grains (lower case b) shows cross-section of a classic hexagonal-trigonal tourmaline shape. Many grains have been broken or are fragments due to, at least in part, the crushing and milling during heavy mineral separation. Photomicrographs of sample MA08 (C), MA24 (D) and BH01 (E) under cross-polarized light and at 45°. See online version for colour.

Figure 3: Tourmaline sample BH05 field photo of quartz-tourmaline stratiform veining with quartz centre (a) and tourmaline growth on edges of vein (b and c). Geological hammer for scale. See online version for colour.

Figure 4: Arrhenius plots for seven tourmaline experiments. The tourmaline diffusion experiments suggest a tourmaline Ar closure temperature of 580°C, with a range of measured closure temperatures between c.a. 490 to 640°C.

Figure 5: Argon age plateaus for tourmaline sample MA08 laser packages (A) and (B) with Cl/K vs. total ^{39}Ar and K/Ca vs. total ^{39}Ar plots. Single grain laser and multi-grain (MG) laser and furnace-diffusion experiments for Mt. Alfred samples MA08 and MA24 and Brooking Hills sample BH05 represented as weighted averages in (C).

Figure 6: A comparison of degassing profiles for hornblende, biotite and tourmaline, minerals with similar T_c ranges to what we propose for tourmaline. (A) Degassing curves measured in the lab, (B) modelled degassing curves.

Figure 7: Argon age plateaus for multi-grain muscovite samples MA05 (A) and BH01 (B) from Mt Alfred and Brooking Hills respectively.

Figure 8: Zircon populations within sample MA08. All uncertainties on ages are given at 2σ . (A) Wetherill diagram showing main concordant age group at 3623 ± 10 Ma; (B) Gaussian probability plot. See online version for colour.

Figure 9: Graphs of boron isotopic results for samples MA24, MA08 and BH04. Histogram in (A) shows most analyses around $\delta^{11}\text{B}$ value of -2.0. Sample MA24 has a broad peak and many analyses below -2.0, sample MA08 shows a bi-polar distribution above and below -4.0, and sample BH04 shows a simple population centering around -1.0. Stacked analyses are shown in graph (B), which shows different fields for the formation of tourmaline. Most of the tourmalines fall within the

carbonates and evaporites field, or also the decompression and prograde field of tourmaline formation. All analyses are enriched in heavy boron versus the continental crust.

Figure 10: Geodynamic history of the Illaara Greenstone Belt with igneous zircon probability histogram on the right (GSWA local dataset compilation) and timeline. Minimum depositional age constraints shown by the sample MA08 $^{40}\text{Ar}/^{39}\text{Ar}$ tourmaline age of 2935 ± 9 Ma. Igneous zircon age peaks correspond with tectono-thermal events (Chen et al., 2003; Chen, Witt, et al., 2001), and post-kinematic intrusions (Chen et al., 2004). Timing of post-deformation quartz veins with associated tourmaline (BH05) is shown as the final event at 2624 ± 16 Ma.

SUPPLEMENTARY INFORMATION

Table A–M: $^{40}\text{Ar}/^{39}\text{Ar}$ data, K/Ca and inverse isochron plots for each aliquot of tourmaline. Table A: MA08, multigrain aliquot. Table B: MA08, multigrain aliquot. Table C: MA08, single grain aliquot. Table D: MA08, single grain aliquot. Table E: MA08, single grain aliquot. Table F: MA08, single grain aliquot. Table G: MA08, single grain aliquot. Table H: MA24, single grain aliquot. Table I: BH01, multigrain aliquot. Table J: BH05, multigrain aliquot. Table K: MA08, multigrain diffusion experiment. Table L: MA08, multigrain diffusion experiment. Table M: BH04, multigrain diffusion experiment. Each table contains multiple tabs that are labeled with their contents including $^{40}\text{Ar}/^{39}\text{Ar}$ results (Relative abundances), age plateau and inverse isochron.

Table N: Table of SHRIMP analytical results for sample MA08

Table O: CONCH Generalized report of boron analysis.

Table P–Q: $^{40}\text{Ar}/^{39}\text{Ar}$ data, K/Ca and inverse isochron plots for each aliquot of muscovite. Table P: MA05. Table Q: BH01.

Figure A.1: Selected degassing curves of data from furnace (blue) and laser (red) experiments.

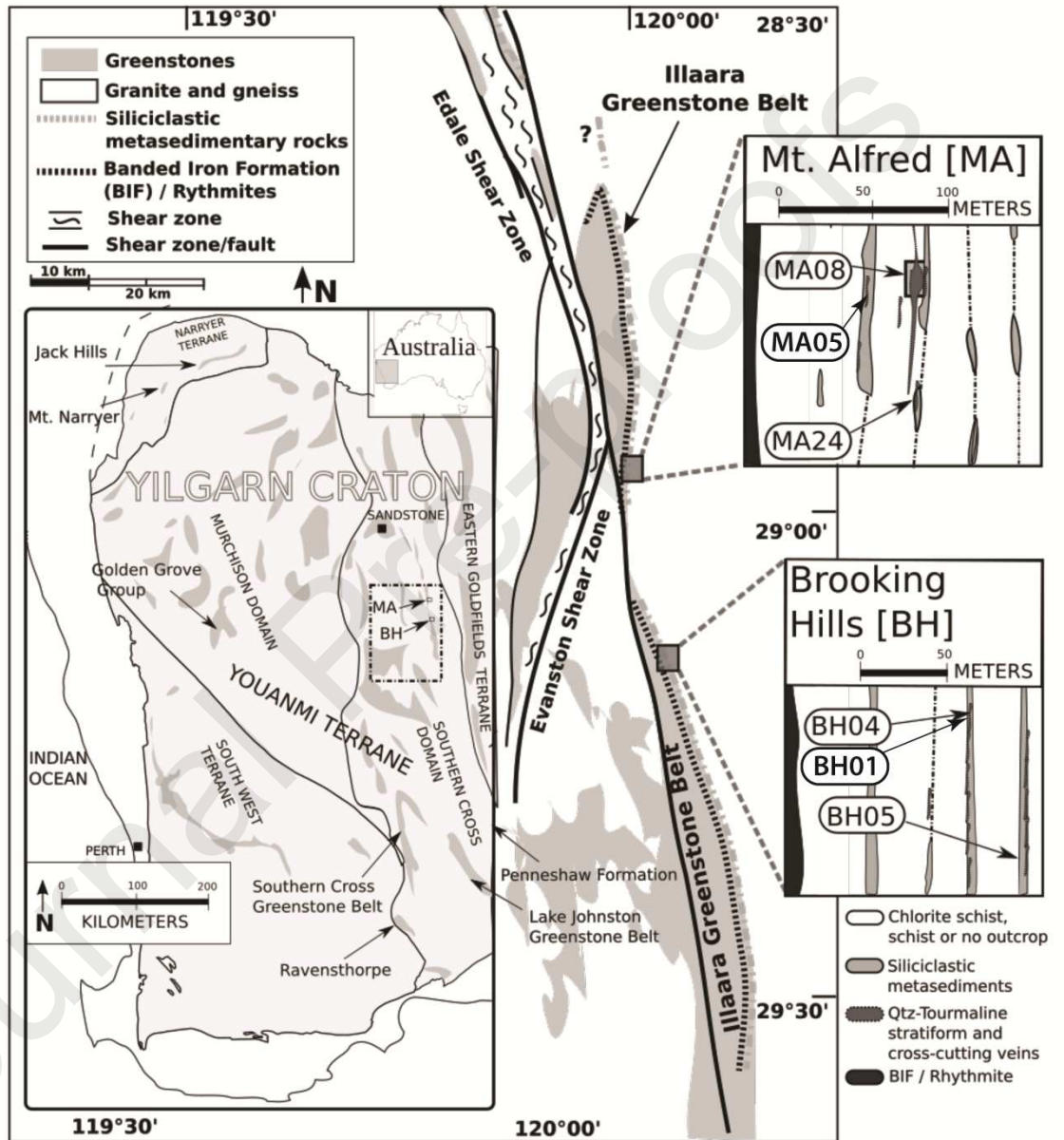
$^{39}\text{Ar}/dT$ represent the amount of gas per temperature (dT) or laser power (dT^*) increment.

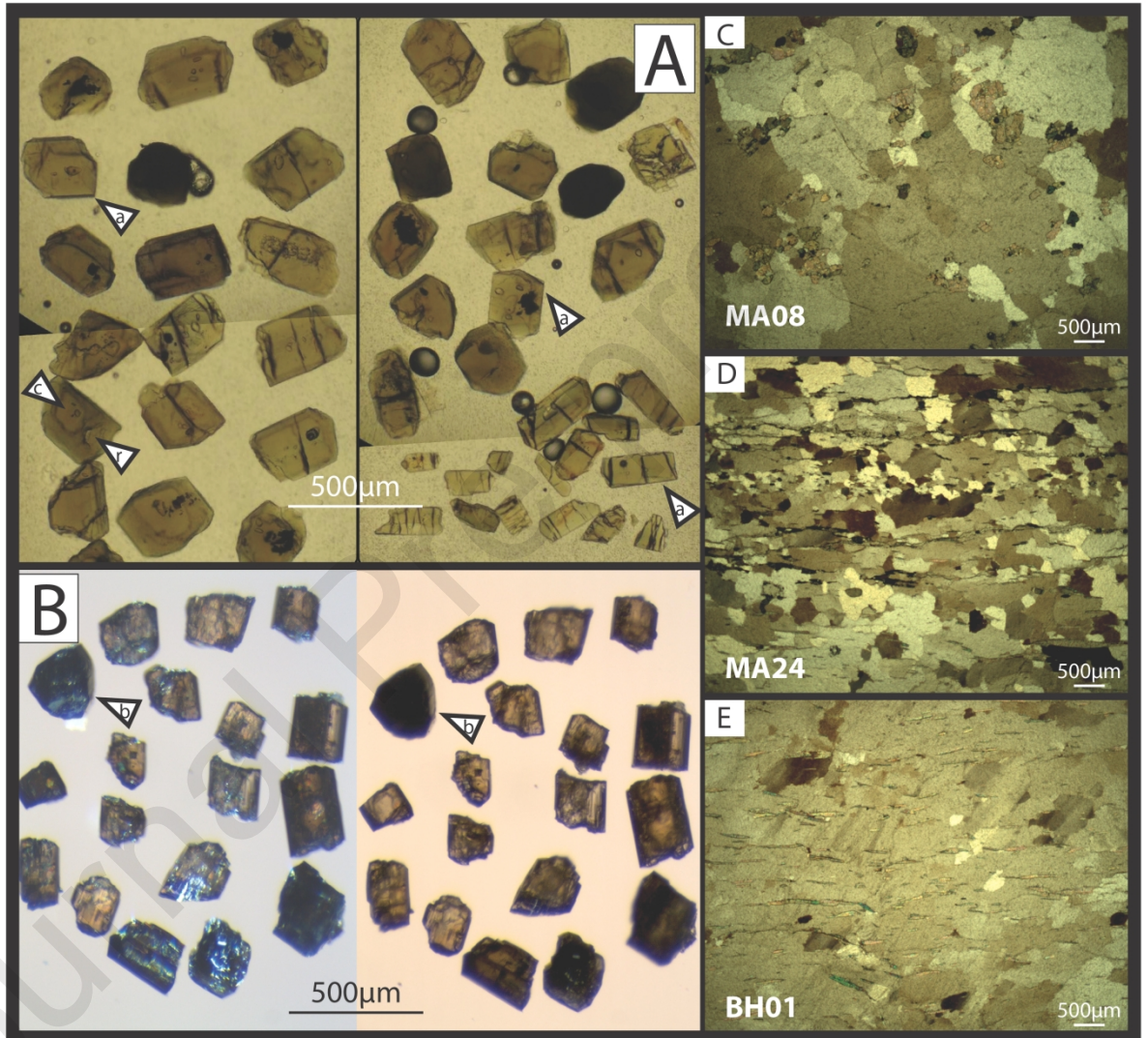
Declaration of interests

The authors declare that they have no known competing financial interests or personal relationships that could have appeared to influence the work reported in this paper.

The authors declare the following financial interests/personal relationships which may be considered as potential competing interests:

Journal Pre-proofs







BH05

